Pergamon

Int. J. Heat Mass Transfer. Vol. 38, No. 4, pp. 701–712, 1995
Copyright © 1995 Elsevier Science Ltd
Printed in Great Britain. All rights reserved
0017–9310/95 $9.50+0.00

0017–9310(94)00185–5

Transient natural convection and conjugate heat transfer in a crystal growth device

C. I. HUNG,† W. SHYY‡ and H. OUYANG

Department of Aerospace Engineering, Mechanics and Engineering Science, University of Florida, Gainesville, FL 32611, U.S.A.

(*Received* 9 *March* 1994 *and in final form* 6 *June* 1994)

Abstract—In crystal growth devices, in order to control the growth defects and compositional homogeneity of the crystal, a thorough understanding of the heat transfer characteristics is required. In this effort, the combined natural convection and conjugate heat transfer in an axisymmetric configuration representative of the container used in float zone devices are numerically simulated. The geometry adopted contains two concentric cylinders, the inner one representing the crystal within which heat conduction takes place, and the outer one being the container wall; between them is the domain of a height-to-width ratio of 40, filled with encapsulated argon gas. The main parameters varied in this study are Rayleigh number (Ra) and heating location. Substantial refinement in grid size, from 61×81 to 201×301 nodes, has been exercised to assess the numerical accuracy of the solutions. For $Ra = 1.25 \times 10^4$, steady-state solutions exist regardless of the heating location. For $Ra = 1.25 \times 10^5$, on the other hand, persistently oscillatory convective patterns appear, exhibiting both co-rotating (buoyancy-induced) cells and contra-rotating (shear-induced) cells. Consequently, the overall heat transfer rates fluctuate in time. The heat transfer fluctuation in the heated region is not as strong as in other regions; however, the magnitudes of the heat flux there are strongly influenced by the heating location, indicating that, in order to maintain a uniform thermal environment, the power level of the heat source needs to be adaptively adjusted according to the heating location. This challenge to the design and operation of the materials processing equipment can be met with the aid of knowledge gained from numerical simulations.

1. INTRODUCTION

Natural convection plays a key role in many crystal growth and alloys casting processes, including Czochralski, Bridgman, float zone, as well as continuous casting [1–3]. A common feature among these diverse processing techniques is the substantial temperature variation within the melt and/or the fluid media (such as argon or B_2O_3) encapsulated in the furnace/container. Prediction of the rates and distribution of heat transfer in these processes is often complicated by the presence of convection. Accordingly, guidance is needed for the design and optimization of thermal conditions within the furnace, including, e.g. coil geometry (for induction heating), thermal scheduling and heater profile. For example, a float zone furnace is schematically depicted in Fig. 1, where, besides the main coil, three preheat zones and three postheat zones are present. Appropriate power distributions of these heaters are critical for: (1) the formation and translation of a stable melt; and (2) control of the growth defects and compositional homogeneity of the crystal. A major goal of this work is to produce information to improve our understanding of the transport processes within a material's solidification device so that better processing techniques can be developed.

In the present effort, the natural convection and conjugate heat transfer phenomena in a device comprised of two concentric circular cylinders are investigated. The geometry, physical dimensions and boundary conditions, illustrated in Fig. 2, represent generically a container within which high temperature melting and solidification take place. The geometry adopted contains two concentric cylinders, the inner one representing the crystal within which heat conduction takes place, and the outer one being the container wall; between them is the domain of a height-to-width ratio of 40, filled with encapsulated fluid. The inner cylindrical rod, with a heated segment moving slowly in time, experiences conduction heat transfer within itself while interacting with the encapsulant (argon is considered here) which separates the rod and the container wall. Within the encapsulated fluid, natural convection takes place due to the temperature difference between the rod and the container wall. Depending on the transport properties, such as thermal diffusivity of the rod and the encapsulant, the location of the heated segment, the range of temperature variation and the size and geometry of the container, different heat transfer characteristics result.

Some primary difficulty in studying the heat transfer characteristics occurring in materials processing devices are the numerous dimensionless parameters,

†Permanent address: Department of Mechanical Engineering, National Cheng Kung University, Tainan, Taiwan.
‡Author to whom correspondence should be addressed.

NOMENCLATURE

g	gravitational acceleration
h	convective heat transfer coefficient
H	heat segment location
k	thermal conductivity of the encapsulant
k_s	thermal conductivity of the rod
l	width of the encapsulant filled region
L	length of the container
L_0	reference length scale
p	dimensionless pressure
P_0	reference pressure scale, α/L_0
Pr	Prandtl number, $\mu/\rho\alpha$
Q	heat flux
r	radial coordinate
R	rod radius
R_0	container radius
Ra	Rayleigh number, $\rho g\beta_T \Delta T l^3/\alpha\mu$
t	dimensionless time
t_0	reference time scale, L_0^2/α
T	dimensionless temperature
T_∞	ambient temperature outside the container
T_{hot}	temperature of the heated segment
T_{ref}	reference temperature of the buoyancy effect
ΔT	reference temperature scale, $T_{hot} - T_\infty$
u	dimensionless radial velocity
U_0	reference velocity scale, α/L_0
w	dimensionless axial velocity
z	axial coordinate.

Greek symbols

α	thermal diffusivity of the encapsulant
α_s	thermal diffusivity of the rod
β_T	coefficient of thermal expansion
ξ	radio, $(R_0 - R)/R$
μ	dynamic viscosity
ρ	characteristic density of the encapsulant.

Subscripts

s	rod
0	reference
∞	ambient.

variations in geometrical configuration and different arrangements of the boundary conditions. Different patterns have been reported qualitatively even in simple geometries [3]. Care needs to be exercised in extrapolating the information reported in the literature for each processing device; issues and conditions encountered should be addressed on a case by case basis. The work reported here investigates the effects

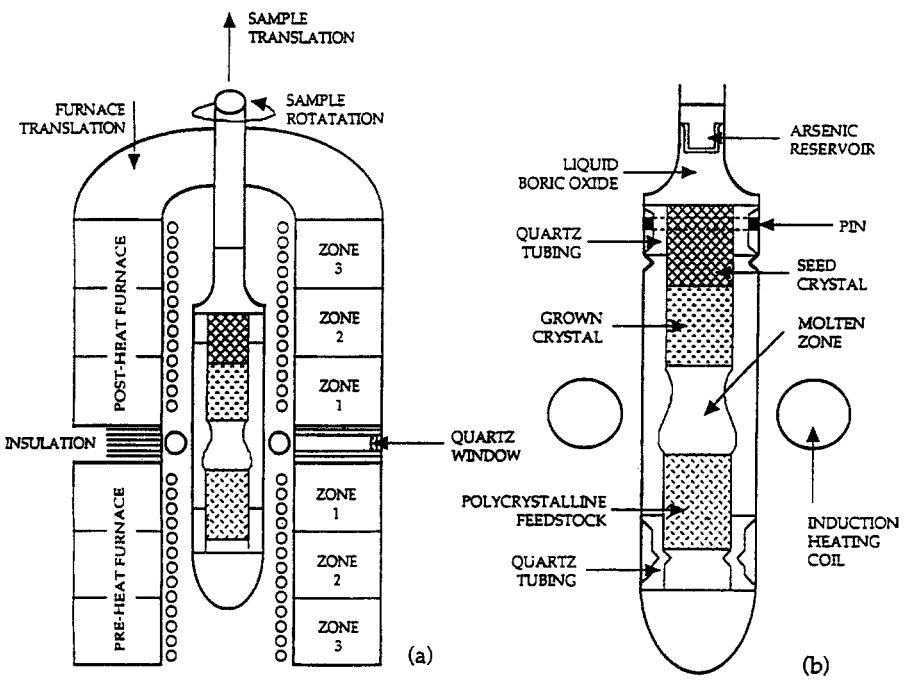

Fig. 1. Schematic of a float zone crystal grower: (a) furnace arrangement; (b) container arrangement.

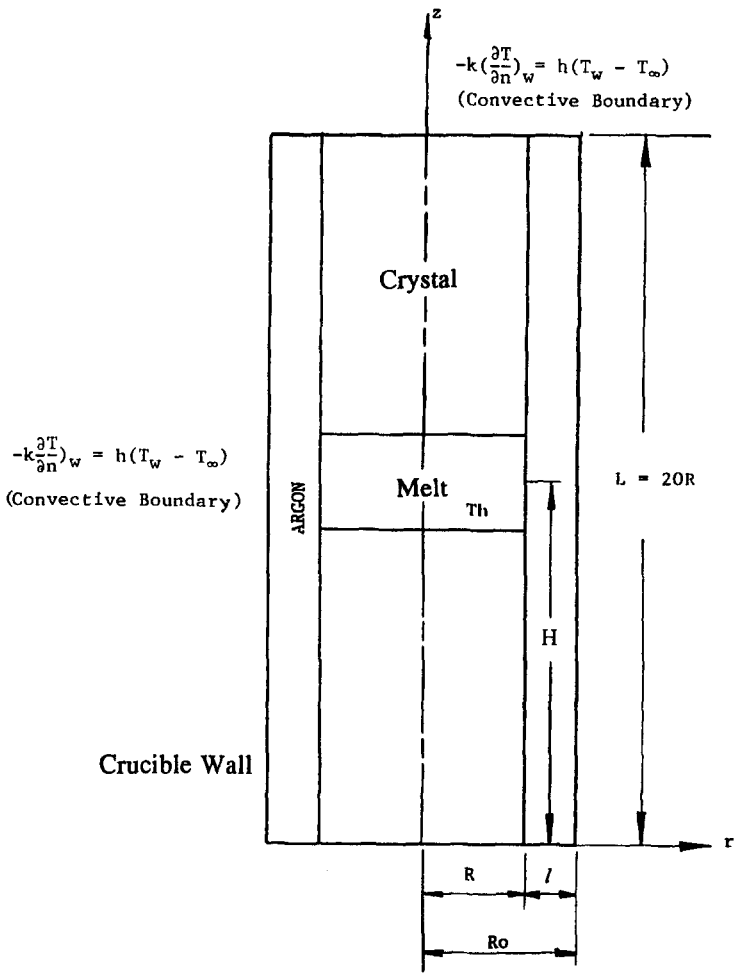

Fig. 2. Schematic of the present axisymmetric model which includes a melt (whose location varies), crystal and argon gas encapsulated inside the container.

of: (1) position of the heated segment; and (2) Rayleigh number on the pattern and distribution of the overall heat transfer. The heat transfer characteristics within the container, including both the rod and the encapsulant, have been studied. The rod, representing the crystal–melt combination, is a circular cylinder of constant radius. The location and the size of the heated segment are fixed so that the number of parameters involved can be reasonably handled. Phase change dynamics are not accounted for here and will be addressed in future study.

2. FORMULATION AND NUMERICAL METHODS

The nondimensionalized transient Navier–Stokes and associated energy equations, with Boussinesq approximation for treating the buoyancy effect, are adopted in a two-dimensional axisymmetric domain. The reference quantities used in the course of nondimensionalization are:

$$\textit{length}: \quad L_0 = R$$

$$\textit{velocity}: \quad U_0 = \frac{\alpha}{L_0}$$

$$\textit{time}: \quad t_0 = \frac{L_0^2}{\alpha}$$

$$\textit{pressure}: \quad P_0 = \rho U_0^2$$

$$\textit{temperature}: \quad \Delta T = T_{\text{hot}} - T_\infty$$

where α is the thermal diffusivity of the encapsulant, R is the rod radius, and the temperature is defined by the difference between the heated segment, maintained at a constant value, T_{hot}, and the ambient temperature outside the container.

First, the nondimensionality governing equations in the encapsulant are given in the following:

(i) *continuity*:

$$\frac{\partial(ru)}{\partial r} + \frac{\partial(rw)}{\partial z} = 0 \tag{1}$$

where u and w are, respectively, the velocity components along the radial and axial direction.

(ii) *radial momentum*:

$$\frac{\partial(ru)}{\partial t}+\frac{\partial(ruu)}{\partial r}+\frac{\partial(rwu)}{\partial z}$$
$$=-r\frac{\partial p}{\partial r}+Pr\left\{\frac{\partial}{\partial r}\left(r\frac{\partial u}{\partial r}\right)+\frac{\partial}{\partial z}\left(r\frac{\partial u}{\partial z}\right)\right\}-Pr\frac{u}{r}. \quad (2)$$

(iii) *axial momentum*

$$\frac{\partial(rw)}{\partial t}+\frac{\partial(ruw)}{\partial r}+\frac{\partial(rww)}{\partial z}$$
$$=-r\frac{\partial p}{\partial z}+Pr\left\{\frac{\partial}{\partial r}\left(r\frac{\partial w}{\partial r}\right)+\frac{\partial}{\partial z}\left(r\frac{\partial w}{\partial z}\right)\right\}$$
$$+r\,Ra\,Pr(T-T_{ref}) \quad (3)$$

where T_{ref} is the reference temperature of the buoyancy effect, i.e. the minimum value of temperature inside encapsulant.

(iv) *energy*:

$$\frac{\partial(rT)}{\partial t}+\frac{\partial(ruT)}{\partial r}+\frac{\partial(rwT)}{\partial z}=\frac{\partial}{\partial r}\left(r\frac{\partial T}{\partial r}\right)+\frac{\partial}{\partial z}\left(r\frac{\partial T}{\partial z}\right). \quad (4)$$

Then, in the solid, the nondimensional governing equation reads:

$$\frac{\partial(rT_s)}{\partial t}=\frac{\alpha_s}{\alpha}\left[\frac{\partial}{\partial r}\left(r\frac{\partial T_s}{\partial r}\right)+\frac{\partial}{\partial z}\left(r\frac{\partial T_s}{\partial z}\right)\right] \quad (5)$$

where α_s and α are, respectively, the thermal diffusivities of the rod and encapsulant.

The nondimensionalized boundary conditions are:

(i) *at symmetrical plane*:

$$\frac{\partial T}{\partial r}=0 \quad (6)$$

(ii) *at outer container boundary*:

$$-\frac{\partial T}{\partial r}=\left(\frac{hR}{k}\right)T \quad (7)$$

(iii) *at top boundary*:

$$-\frac{\partial T}{\partial z}=\left(\frac{hR}{k}\right)T \quad \text{for encapsulant}$$
$$-\frac{\partial T}{\partial z}=\left(\frac{hR}{k_s}\right)T \quad \text{for solid} \quad (8)$$

(iv) *at bottom boundary*:

$$\frac{\partial T}{\partial z}=\left(\frac{hR}{k}\right)T \quad \text{for encapsulant}$$
$$\frac{\partial T}{\partial z}=\left(\frac{hR}{k_s}\right)T \quad \text{for solid} \quad (9)$$

where k_s and k are, respectively, thermal conductivity of the rod and encapsulant, and h is the convective heat transfer coefficient. For all the cases considered in this paper, in the encapsulated region, the value of the dimensionless group, (hR/k), is taken as 0.265; for the rod, the value of (hR/k_s) is 2.46×10^{-4}, due to the fact that the thermal conductivities of encapsulant and rod differ by a factor of 1077.

Table 1. Parameters used in the present study

(a) Thermal properties
Rod/encapsulant thermal diffusivity ratio = 0.147
Rod/encapsulant thermal conductivity ratio = 1077

(b) Dimensionless transport parameters
Prandtl number = 0.66
Rayleigh number = 1.25×10^4 and 1.25×10^5

(c) Geometry
Height of container (L)/rod radius (R) = 20
Container radius (R_0)/rod radius (R) = 1.5
Height of heated segment/rod radius = 1.0

(d) Position of heated segment/height of container (center to center) 1/8, 1/2

In the present case, radiation heat transfer mainly serves to modify the boundary conditions; it is not considered here. The key parameters appear in the problem formulation, summarized in Table 1.

(i) *Aspect ratios of the rod and encapsulant, and geometry of container*

A schematic of the geometry is shown in Fig. 2, in which $L/R=20$, and $\xi=(R_0-R)/R=0.5$, where L is the length of the container, and R and R_0 are, respectively, radii of the rod and the container.

(ii) *Thermal Rayleigh number*

$$Ra=\frac{\rho g\beta_T\Delta T l^3}{\alpha\mu} \quad (10)$$

where g is gravitational acceleration, ρ is the characteristic density of the encapsulant, l is the width of the encapsulant filled region, ΔT is the characteristic temperature variation in the encapsulant, β_T is the coefficient of thermal expansion, μ is the dynamic viscosity and α is the thermal diffusivity of the encapsulant.

(iii) *Prandtl number.*

$$Pr=\frac{\mu/\rho}{\alpha}.$$

(iv) *Ratios of thermal diffusivity and heat conductivity between the rod and encapsulant.*

(v) *Position and height of the heated segment.*

The reference time-scale used for nondimensionalization is R^2/α, where R is rod radius and α is thermal diffusivity of the encapsulant; for the present configuration, this time-scale is 0.23 s. Transient computations have been conducted to simulate the development and evolution of the thermal and fluid flow characteristics within the container. Since

in practice the heated segment, which represents the melting zone, moves at a very slow pace, typically of the order of 10^{-1} (for single crystal growth) to 1 (for continuous ingot casting) m h^{-1}, the convection and heat transfer processes can be simulated using a quasi-steady boundary condition. Accordingly, one can conduct a series of transient simulations by considering the heat source to be stationary at different locations in time.

Initially, both the container wall and argon encapsulant are set at a constant temperature, $T = 0$, while the rod is of a linear profile, with $T = 1$ in the heated segment and $T = 0$ at both ends. In the course of simulation, heat flux conditions are assigned on all sides of the container, as depicted in Fig. 2. The temperature in the heated segment is maintained at $T = 1$ at all time. In the rod, the temperature distribution is determined by solving the heat conduction equation. At the rod–argon interface, heat flux is balanced from both sides. To appropriately handle the large disparity of the thermal conductivities between the rod and the encapsulant, one can use either an explicit heat flux balance or an effective thermal conductivity based on the harmonic average of the thermal conductivities of the two sides of the interface; both treatments yield virtually the same results [4, 5]. In the present study, the harmonic mean approach has been adopted. The solution techniques adopted here is based on the well established SIMPLE algorithm [4]. The grid arrangement is based on the orthogonal coordinate system. Extension to the nonorthogonal coordinates has also been well developed, as detailed in Shyy [3]. Second-order central difference discretization schemes have been adopted for all the spatial terms unless otherwise stated, and backward Euler time stepping is employed for the temporal terms.

Many computations have been conducted on different grid sizes, for various Rayleigh numbers and locations of the heated segment. The grid size ranges from 61 (radial) $\times$ 81 (axial) to 201×301 nodes. Within both the rod and the encapsulant, the grid is distributed nonuniformly along the radial direction. For the coarse, 61×81, grid, 21 grid points are assigned in the rod; for the fine, 201×301, grid, 41 grid points are in the rod. The grid layout is governed by a cubic polynomial, with the boundary locations and the end grid spacings in each domain specified. For example, with 61×81 grid, the end grid spacing at both ends is 9.6×10^{-3} for encapsulant, and is 6.7×10^{-2} for rod; with 201×301 grid, on the other hand, the spacings are, respectively, 3.4×10^{-5} and 1.9×10^{-2}. Along the axial direction, the grid is uniformly distributed.

3. RESULTS AND DISCUSSION

3.1. Ra $= 1.25 \times 10^4$

We first present the case of $Ra = 1.25 \times 10^4$; again, the Rayleigh number is defined based on the dimension of the width of the encapsulant filled region. First,

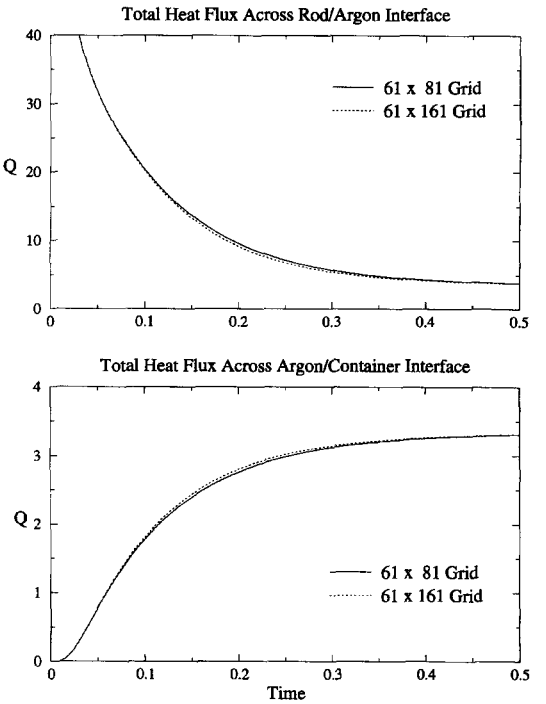

Fig. 3. Assessment of grid dependency and transient behavior, $H = 1/8$, $Ra = 1.25 \times 10^4$.

to assess the solution accuracy, Fig. 3 shows the total heat fluxes through the rod–encapsulant interface and the encapsulant–container interface on two grids, 61×81 and 61×161 nodes, with the heated segment located at 1/8 height from the bottom of the container. The dimensionless total heat flux, Q, is defined by:

$$Q = \int_0^L \left(-r\frac{\partial T}{\partial r}\right) dz \tag{11}$$

where the two-point one-sided difference scheme is used for estimating the temperature gradient as well as for making the integration.

As demonstrated in Fig. 3, at this Rayleigh number, it is not difficult to obtain accurate solutions even with a modest grid size. Steady state is reached monotonically within a nondimensional time of 0.5. It is noted that the reference time-scale used in nondimensionalization is based on the conductive characteristic time, which is obviously very large compared to that controlling the dynamics of the transport process within the whole container. Since the ratio of convective and viscous time-scales is proportional to the square root of Grashof number, the velocity field is expected to settle down quickly if steady-state solutions exist. Figure 4 compares the stream functions and isotherm contours of the steady-state solutions obtained on the two grids. The two solutions are very close to each other; a single recirculating cell is present in the convection field and the thermal distribution resembles that of a purely conductive field. The buoyancy effect is more noticeable in the region next to the

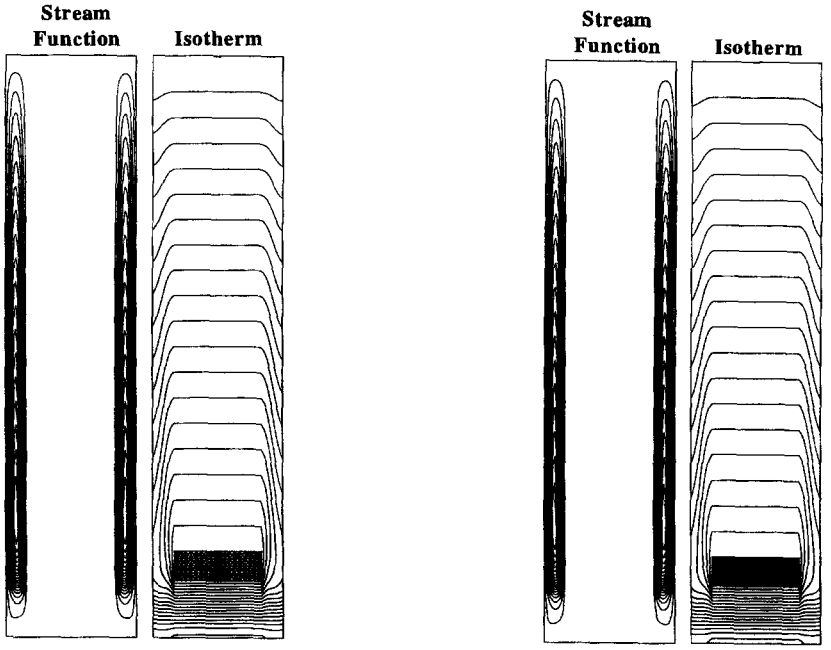

Fig. 4. Effect of grid resolution on solution characteristics with $H = 1/8$, $Ra = 1.25 \times 10^4$ at steady state.

heated segment as evidenced by the distortion of the isotherms there. Due to the large difference in thermal conductivities, temperature gradients exhibit abrupt changes across the rod–encapsulant interface.

Regarding the effect of the heating location on the overall heat transfer rate, Fig. 5 compares the time histories of the total heat fluxes for $H = 1/8$ and $1/2$. The total heat fluxes across the rod–encapsulant and encapsulant–container interfaces in both cases closely follow each other at all time, and the overall strengths of the stream function corresponding to $H = 1/8$ (Fig. 4) and $H = 1/2$ (Fig. 6) are very comparable. Consequently, although the thermal boundary conditions of the two cases are different, and the thermal characteristics respond to the change accordingly, the total heat fluxes are not noticeably affected.

3.2. Ra $= 1.25 \times 10^5$

Next we consider the case of $Ra = 1.25 \times 10^5$. Steady-state solutions have been reported for comparable Rayleigh number with high Prandtl fluids inside containers of aspect ratios far away from unity, see e.g. De Vahl Davis and Mallinson [6], as well as for quite comparable Rayleigh and Prandtl numbers in a different enclosure with two parallel heated plates [7]. The critical values of these dimensionless parameters are, obviously, configuration and boundary conditions dependent. In the present configuration, steady state does not exist for $Ra = 1.25 \times 10^5$. Figure 7 first compares the effect of grid resolution on the solution characteristics in terms of time histories of the total heat fluxes computed on three different grid systems, namely, 61 (radial) $\times$ 161 (axial), 121×201 and 201×301 nodes. It is interesting to observe that, for $Ra = 1.25 \times 10^4$, accurate solutions can be obtained on quite a coarse grid consisting of 61×81 nodes. For the present Rayleigh number, however, even with much refined resolution, the solutions exhibit substantial variations from one grid to another. It should be emphasized that by varying the grid distribution, not only the quantitative aspects of the solutions vary but also the qualitative pattern of each simulation change. This finding indicates that, with the present geometry and Rayleigh number, details of the transport process are prone to noises created during the simulation and are highly path dependent. The subject of oscillatory natural convection has attracted much attention in the last several decades from both engineering and physics communities [8–11]. It is known that steady-state multiple solutions exist for buoyancy-induced transport under identical boundary conditions [12, 13].

A large number of references related to natural convection in tall containers can be found in Gebhart *et al.* [9], Lee and Korpela [14], Le Quere [15] and Hyun [16]. In the present case, unsteady convection persists after the single cell convection becomes multiple-cell as the Rayleigh number increases from 10^4 to 10^5. Under such circumstances, the time dependent convection apparently does not extend coherently through the entire convection chamber [10, p. 102]; in other words, convection cells do not oscillate synchronously over the entire domain of the container [17, 18]. Although the boundary conditions, geometry

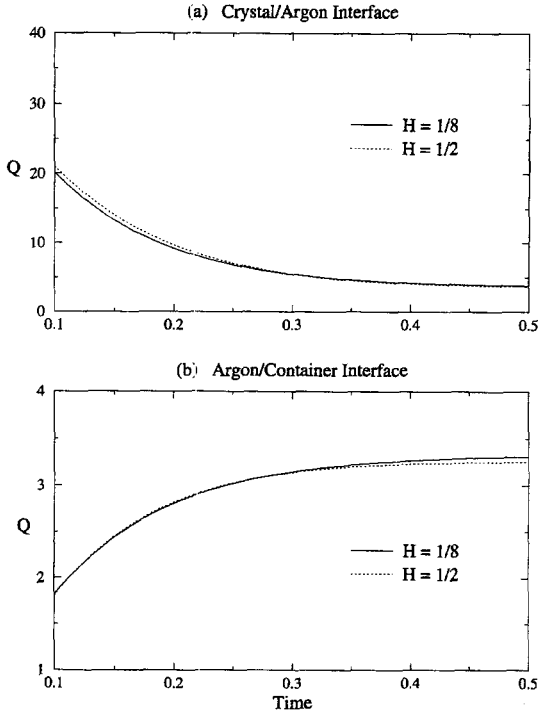

Fig. 5. Time history of total heat flux through: (a) crystal–argon interface; (b) argon–container interface ($Ra = 1.25 \times 10^4$, grid size = 61×161).

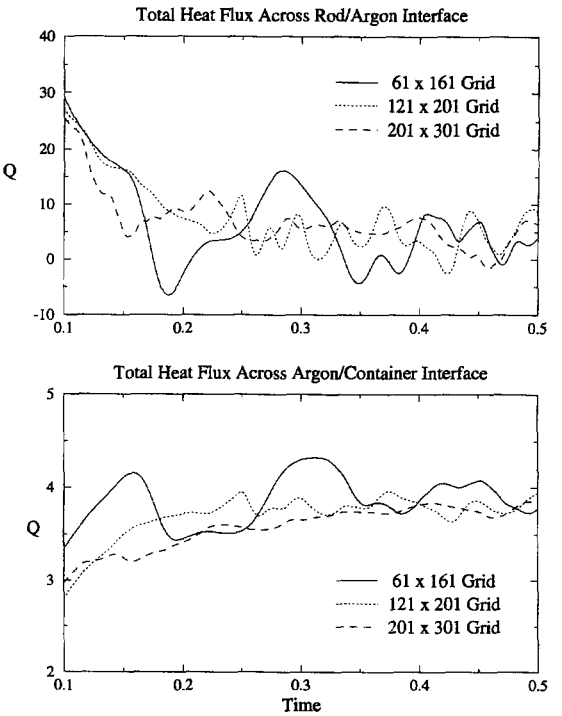

Fig. 7. Assessment of grid dependency and transient behavior, $H = 1/8$, $Ra = 1.25 \times 10^5$.

and material properties considered here are different from these cited studies, the non-coherent pattern of the solutions, in space as well as in time, is clearly observable. To demonstrate the irregular characteristics of the solutions, Fig. 8 depicts the stream function and isotherm contours on three different grids, including 61×161, 121×201 and 201×301 nodes, at the time instant $t = 0.5$. The number of convection cells, the overall and relative strengths of these cells and the corresponding isotherm distributions are different on all grid systems; no apparent regularity in pattern formation exists even with much refined grids.

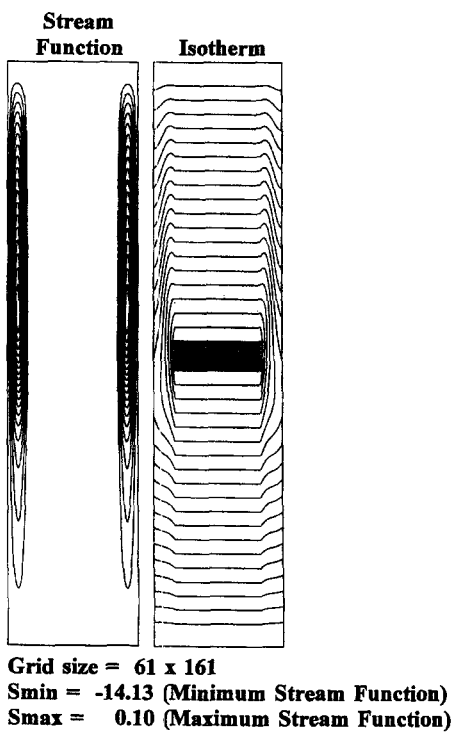

Fig. 6. Stream function and isotherm distributions at steady state with $H = 1/2$ and $Ra = 1.25 \times 10^4$.

Figure 9 shows the evolution of the convective and thermal characteristics obtained on the 201×301 grid at time $t = 0.2$, 0.3 and 0.4 which portrays a progressive evolution in transport patterns. The system clearly exhibits irregular features in both convective and thermal fields. Figures 8 and 9 show that merger and break-up of the convective cells can be observed. Furthermore, the convective field contains both contra-rotating and co-rotating cells. The formation of contra-rotating cells requires the fluid in some cells to move upward along the container wall, which initially is colder, and downward along the rod, which initially is hotter, creating an environment which is unstable from the buoyancy point of view. For the co-rotating cells, on the other hand, the velocity vectors are along the opposite direction across the interface between the two neighboring convection cells, causing excessive shear forces compared to the contra-rotating cells, thus creating a situation which is not conducive for maintaining the shear stability. Rogers and Yao [19] have recently analyzed natural convection in a heated vertical concentric annulus with the inner cylinder

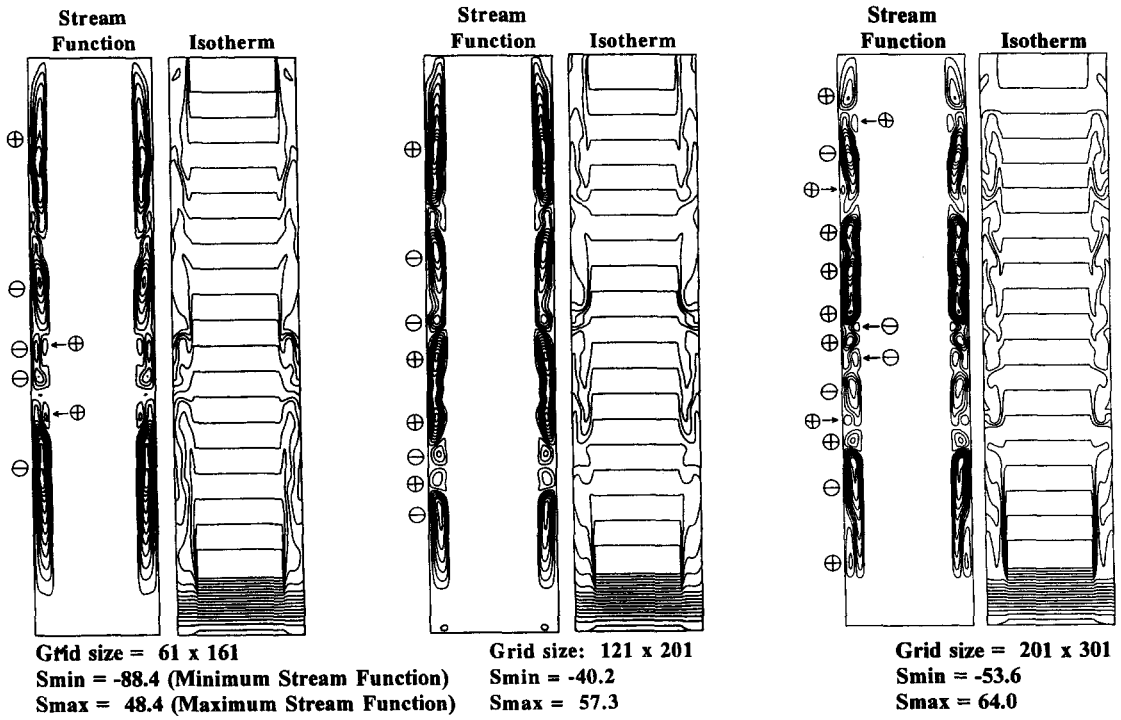

Fig. 8. Effect of grid resolution on solution characteristics with $H = 1/8$, $Ra = 1.25 \times 10^5$ and time = 0.5 ($\oplus$ indicates counterclockwise rotation, $\ominus$ indicates clockwise rotation).

subject to constant heat-flux and outer cylinder subject to adiabatic conditions. Based on linear and weakly nonlinear stability analyses they reported that when the Prandtl number is small, $O(10^{-1})$ or lower, dominant instability obtains energy primarily from shear production; when the Prandtl number is large, O(10) or higher, however, an instability that obtains kinetic energy from buoyant production is dominant.

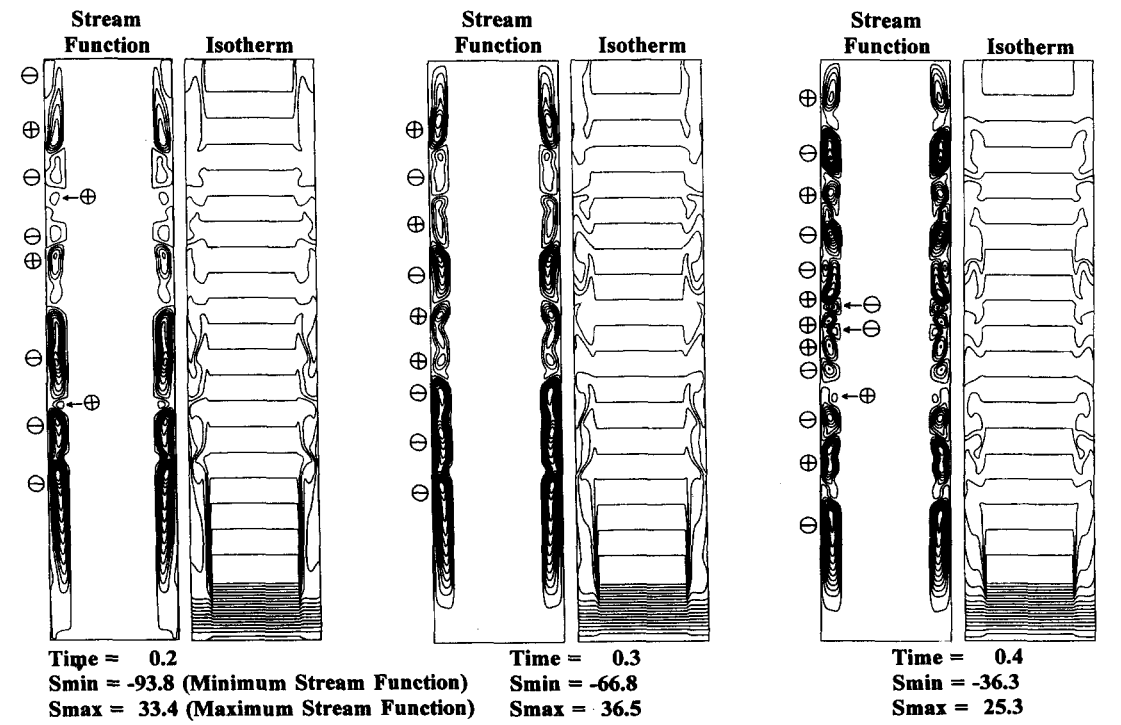

Fig. 9. Stream function and isotherm distributions on 201 x 301 grid at three different time instants with $H = 1/8$ and $Ra = 1.25 \times 10^5$ ($\oplus$ indicates counterclockwise rotation, $\ominus$ indicates clockwise rotation).

The Prandtl number considered in the present investigation is intermediate. It is interesting to observe that both buoyancy-induced (co-rotating) cells and shear-induced (contra-rotating) cells appear; Fig. 9 shows that an initially long convection cell, containing multiple co-rotating cells within it, first experiences a break-up to form contra-rotating cells of smaller length scales. These secondary, and tertiary cells can also merge at a later stage to form larger cells. Physics relevant to these aspects has been studied experimentally by Chen and Wu [20] in a different configuration with high Prandtl number fluids.

Figure 10 assesses the impact of the location of the heated segment on the time histories of the total heat fluxes; as expected, the heating location now plays a substantial role in determining the heat transfer characteristics. Highly irregular temporal trends are observed with both heating locations. The merger–break-up processes just described and the continually varying cell sizes in the convective field are responsible for the multiple time-scales present in the plots. Figure 11 shows convective and thermal fields on a 121×201 grid at $t = 0.3$, 0.4 and 0.5 for $H = 1/2$. Similar to the case of $H = 1/8$, merger and break-up of the convection cells continually appear. To offer more insight into the key features of the heat transfer process, Fig. 12 shows the heat flux distribution through the rod–encapsulant and encapsulant–container interfaces at selected time instants, with both $H = 1/8$ and $1/2$ for $Ra = 1.25 \times 10^5$. Because the sizes of these convective cells are dictated by the position of the heated segment and can vary substantially in time, the distributions of heat fluxes through the rod as well as the container wall fluctuate noticeably. Furthermore, convection causes heat to flow from encapsulant into the rod in the upper domain of the container with both heating locations. Since the heated segment is the source of buoyancy-induced convection, the isotherms are always concentrated in its vicinity. Away from the heated segment, the convection cells vary in size and strength, causing the fluid to change speed and direction continually. This unsteadiness is responsible for the substantial variations in heat transfer characteristics depicted in Fig. 12. More importantly, between $H = 1/8$ and $1/2$, the magnitudes of heat flux through the rod are very different. With $H = 1/8$, heat fluxes from the heated segment are substantially higher than those with $H = 1/2$. According to Figs. 8, 9 and 11, the *overall* convective strength with $H = 1/8$ is not higher than that with $H = 1/2$; however, the *local* convective strength in the heating region with $H = 1/8$ is higher.

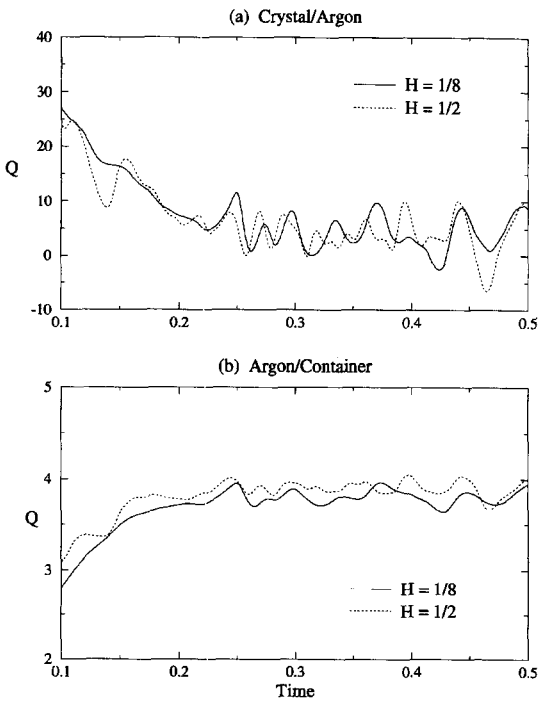

Fig. 10. Effect of the location of heated segment on the time history of total heat flux through: (a) crystal–argon; (b) argon–container with $Ra = 1.25 \times 10^5$, grid size = 121×201.

Finally, Fig. 13 shows the corresponding information of heat transfer distribution along the interfaces with $H = 1/8$ and $1/2$, and for $Ra = 1.25 \times 10^4$. Consistent with the results already presented, for both heating locations, the system approaches steady state, as evidenced by the closeness of the heat flux profiles between $t = 0.4$ and 0.5. Furthermore, at all time instants, the heat flux profiles with $Ra = 1.25 \times 10^4$ exhibit a single peak at the location where the heated segment is located. In contrast, with $Ra = 1.25 \times 10^5$, multiple peaks are present because of the merger and break-up processes in the convective field.

Based on the solutions obtained here, one can draw information relevant to materials solidification devices. For example, to control the uniformities of the solidified material, the phase change process should be allowed to proceed in a steady manner. Hence, the finding that heat transfer fluctuation in the heating region, where the phase change process takes place, is not as strong as in other regions is desirable. However, one also observes that the magnitudes of heat flux out of the heated segment are strongly influenced by the location of heat source, indicating that, in order to maintain a stable thermal environment, power put into the heat source needs to be adaptively adjusted as it moves up and down. This finding clearly poses a challenge to the design and operation of the materials processing equipment.

4. CONCLUSION

1. The combined natural convection and conjugate heat transfer in an axisymmetric configuration representative of the container used in float zone devices are numerically simulated. The main parameters investigated are Rayleigh number and heating location.
2. Substantial variations in grid distributions, ranging from 61×81 to 201×301, have been made to assess

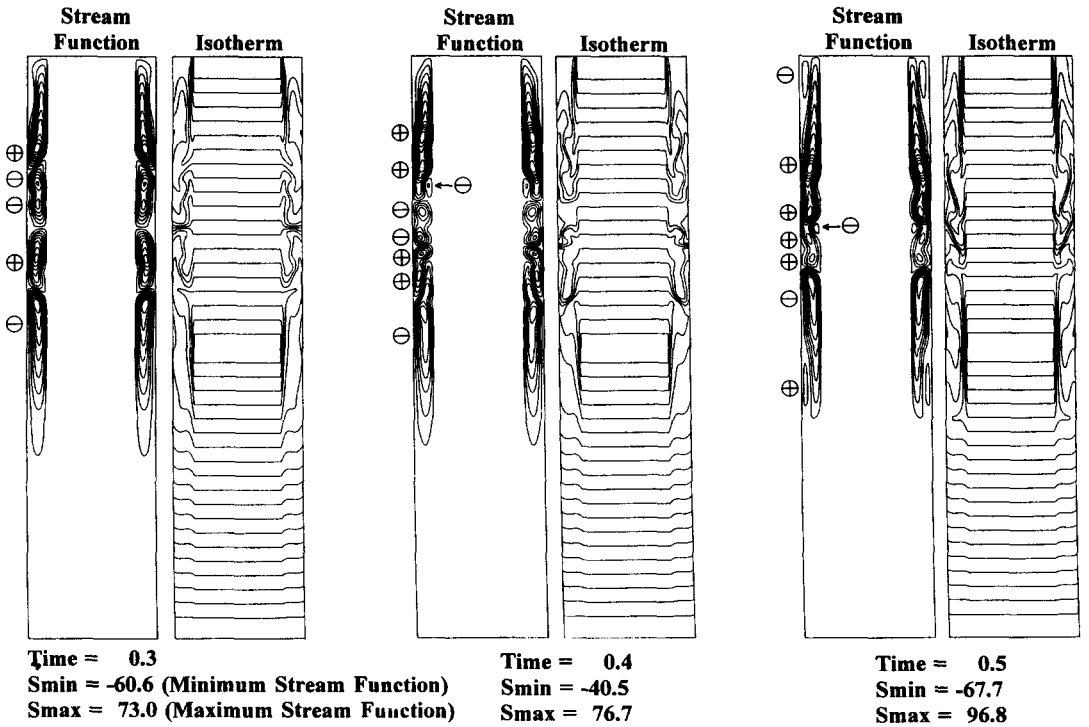

Fig. 11. Stream function and isotherm distributions on 121×201 grid at three different time instants with $H = 1/2$ and $Ra = 1.25 \times 10^5$ ($\oplus$ indicates counterclockwise rotation, $\ominus$ indicates clockwise rotation).

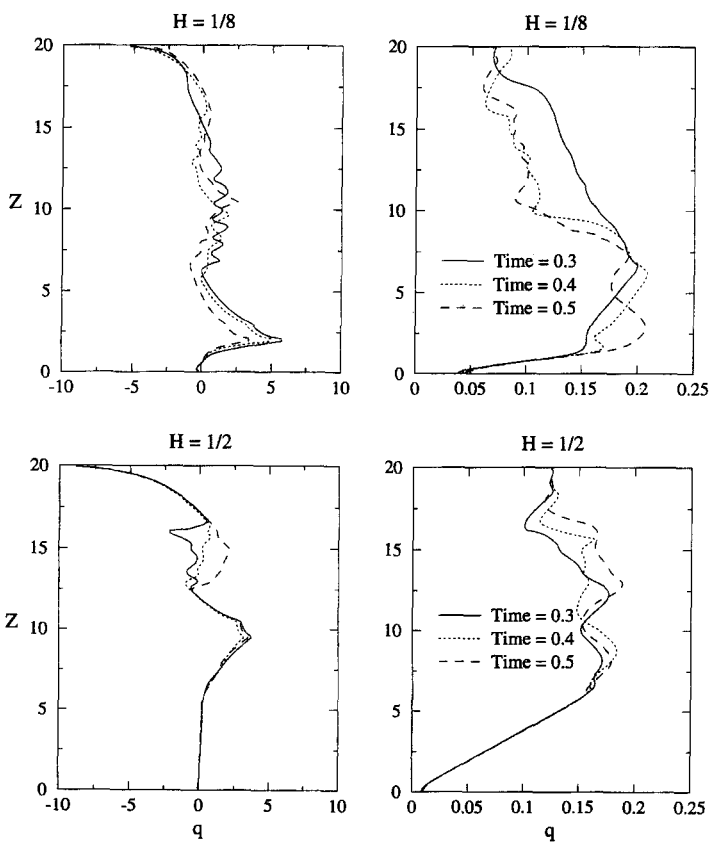

Fig. 12. Distribution of heat flux through: (a) crystal–argon; (b) argon–container at selected time instants ($Ra = 1.25 \times 10^5$, grid size = 61×161).

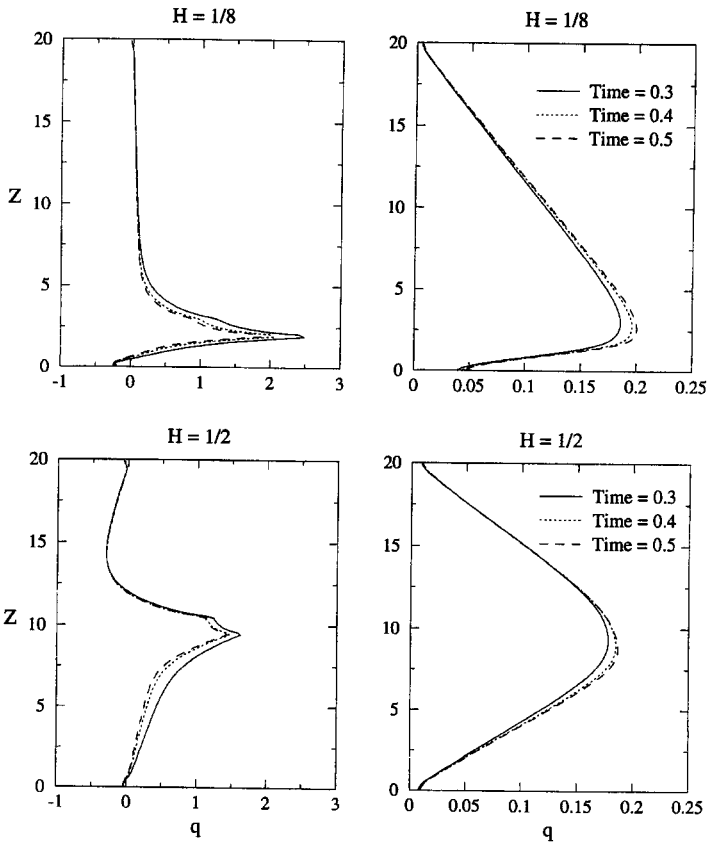

(a) Crystal/Argon (b) Argon/Container

Fig. 13. Distribution of heat flux through: (a) crystal–argon; (b) argon–container at selected time instants ($Ra = 1.25 \times 10^4$, grid size = 61×161).

the numerical accuracy of the solutions. Due to the large difference of heat conductivity between the rod and encapsulant, a factor of 1077, the isotherms exhibit different slopes across the rod–encapsulant interface for all cases.

3. For $Ra = 1.25 \times 10^4$, steady-state solutions can be obtained with modest grid resolutions, regardless of the heating location. The overall heat transfer rates seem to be insensitive to the heating location, indicating that, from a convection point of view, the furnace can operate without detailed thermal scheduling.
4. For $Ra = 1.25 \times 10^5$, however, the transport processes are prone to noises created during the simulation.
   (i) Persistently oscillatory convective patterns appear, which exhibit both co-rotating (buoyancy-induced) cells and contra-rotating (shear-induced) cells. Consequently, the overall heat transfer rates fluctuate as function of time and heating location.
   (ii) The heat transfer fluctuation in the heating region, where the phase change process takes place, is not as strong as in other regions, which is desirable.
   (iii) Although the total heat fluxes (Fig. 10) do not seem to exhibit a strong dependency of the heating location, the distributions as well as magnitudes of the heat flux are qualitatively different between $H = 1/8$ and $1/2$. This finding indicates that, in order to maintain a stable melt size and shape, the power level of heat source needs to be adaptively adjusted.

The findings of the high Ra cases pose a challenge to the design and operation of the materials processing equipment. The computer-aided control schemes can be devised based on the information obtained from the present computations.

Acknowledgments—This work has been partially supported by the AFOSR University Research Initiative Program and the National Science Council of the Republic of China. The computations were conducted on Cray Y-MP at Eglin Air Force Base and Cray C916/16512 at the Army Corps of Engineers WES Supercomputer Center at Vicksberg (MS). Discussions held with Professors Reza Abbaschian and Michael Kaufman of the Department of Materials Science and Engineering, University of Florida, have been very helpful.

REFERENCES

1. J. C. Brice, *Crystal Growth Processes*. Blackie, London (1986).

2. R. A. Brown, Theory of transport processes in single crystal growth from the melt, *A.I.Ch.E. Jl* **34,** 881–911 (1988).
3. W. Shyy, *Computational Modeling for Fluid Flow and Interfacial Transport*. Elsevier, Amsterdam (1994).
4. S. V. Patanka, *Numerical Heat Transfer and Fluid Flow*. Hemisphere, Washington, DC (1980).
5. W. Shyy and J. Burke, A study of iterative characteristics of convective–diffusive and conjugate heat transfer problems, *Numer. Heat Transfer* **26,** 21–37 (1994).
6. G. De Vahl Davis and G. D. Mallinson, A note on natural convection in a vertical slot, *J. Fluid Mech.* **72,** 87–93 (1975).
7. W. Shyy and M. M. Rao, Simulation of transient natural convection around an enclosed vertical channel, *J. Heat Transfer* **115,** 946–954 (1993).
8. P. Berge, Y. Pomeau and C. Vidal, *Order within Chaos*. Hermann, Paris (1984).
9. B. Gebhart, Y. Jaluria, R. L. Mahajan and B. Sammakia, *Buoyancy-induced Flows and Transport*. Hemisphere, Washington, DC (1988).
10. E. L. Koschmieder, *Benard Cells and Taylor Vortices*. Cambridge University Press, Cambridge (1993).
11. K. T. Yang, Transitions and bifurcations in laminar buoyant flows in confined enclosures, *J. Heat Transfer* **110,** 1191–1204 (1988).
12. M. E. Braaten and S. V. Patankar, Analysis of laminar mixed convection in shrouded arrays of heated rectangular blocks, *Int. J. Heat Mass Transfer* **28,** 1699–1709 (1985).
13. W. Shyy and M.-H. Chen, A study of the transport process of buoyancy-induced and thermocapillary flow of molten alloy, *Computer Meth. Appl. Mech. Engng* **105,** 333–358 (1993).
14. Y. Lee and S. A. Korpela, Multicellular natural convection in a vertical slot, *J. Fluid Mech.* **126,** 91–121 (1983).
15. P. Le Quere, Transition to unsteady natural convection in a tall water-filled cavity, *Phys. Fluids A* **2,** 503–515 (1990).
16. J. M. Hyun, Unsteady buoyant convection in an enclosure. In *Advances in Heat Transfer* (Edited by J. P. Hartnett, T. F. Irvine, Jr and Y. I. Cho), Vol. 24, pp. 277–320. Academic Press, New York (1994).
17. J. P. Gollub and S. V. Benson, Chaotic response to periodic perturbation of a convecting fluid, *Phys. Rev. Lett.* **41,** 948–951 (1978).
18. A. Libchaber and J. Maurer, Local probe in a Rayleigh–Benard experiment in liquid helium, *J. Phys. Lett.* **39,** 369–372 (1978).
19. B. B. Rogers and L. S. Yao, Natural convection in a heated annulus, *Int. J. Heat Mass Transfer* **36,** 35–47 (1993).
20. F. Chen and C. H. Wu, Unsteady convective flows in a vertical slot containing variable viscosity fluids, *Int. J. Heat Mass Transfer* **36,** 4233–4246 (1993).